Chemistry – A European Journal

ChemEurJ Chemistry Europe European Chemical Societies Publishing

RESEARCH ARTICLE

An Au_{25} Nanocluster-Based Electrochemical Biosensor for Profenofos Detection With High Activity and Sensitivity

Yuying Zhang[1] | Jianfang Qin[1] | Mengxi Zhang[1] | Lijuan Jia[1] | Fenglin Zhang[1] | Tong Chang[1] | Haiying Yang[1] | Xu Liu[2,3] | Yan Zhu[2]

[1]Department of Applied Chemistry, Yuncheng University, Yuncheng, Shanxi, China | [2]State Key Laboratory of Coordination Chemistry, Key Laboratory of Mesoscopic Chemistry of the Ministry of Education, School of Chemistry and Chemical Engineering, Nanjing University, Nanjing, Jiangsu, China | [3]Institute For Energy Research, Jiangsu University, Zhenjiang, Jiangsu, China

Correspondence: Haiying Yang (hyyang@ycu.edu.cn) | Xu Liu (xuliu@nju.edu.cn) | Yan Zhu (zhuyan@nju.edu.cn)

Received: 5 January 2026 | **Revised:** 15 April 2026 | **Accepted:** 20 April 2026

Keywords: Au_{25} cluster | electrochemical sensor | enzyme inhibition | profenofos detection

ABSTRACT

Exploiting atomic-precision metal nanoclusters as an electrochemical sensor for environmental detection is a significant application in the field of cluster chemistry. However, the development of cluster-based sensors is still in its infancy. Herein, we successfully fabricate a three-layer KBE-CS/Au_{25}@MLG/GC electrode (KBE = kidney bean enzyme, CS = chitosan, MLG = multilayer graphene, GC = glassy carbon), in which Au_{25}@MLG and CS serve to adsorb and protect the plant esterase of KBE, respectively. The optimized Au_{25}-based sensor demonstrates an excellent linear relationship between the mass concentration of profenofos (lgC) and the inhibition rate (Inh %) within the range of 1∼2000 μg/L with a detection limit of 0.137 μg/L. Furthermore, this biosensor presents excellent reproducibility, anti-interference, and stability for the detection of profenofos in real samples. This study paves an avenue to construct a cluster-based detection platform with high performance in electrochemical sensing, facilitating the practical application of metal nanoclusters in pesticide detection.

1 | Introduction

As a new type of nanomaterial with a well-defined structure, atomically precise metal nanoclusters have spurred an increasing interest in the realm of nanoscience and nanotechnology due to unique physicochemical properties [1–6]. For instance, the ultra-small size of metal nanoclusters (≤3 nm) close to the Femi wavelength gives rise to discrete energy levels and thus leads to molecule-like optical absorption rather than surface plasma resonance (SPR), which is frequently observed in metal nanoparticles with a size of ≥5 nm. Furthermore, the structural adjustability of metal nanoclusters by atomic-scale modification allows them to serve as an ideal platform to establish the relationship between molecule-like properties and the structure [7–10]. Because of distinctive and excellent properties, metal nanoclusters exhibit a huge potential in fields of optics, chirality, biomedicine, and catalysis [11–22]. In addition to the fields mentioned above, remarkable achievements have recently been acquired in the sensing application of metal nanoclusters. A series of nanocluster-based photochemical sensors have successfully been constructed on the basis of their photoluminescent property, which are subsequently utilized to detect molecules or ions [23–25]. For example, Anu George and his colleagues constructed self-standing films using highly luminescent Au_{15} clusters to detect Cu^{2+} ions with a sensitivity of 1 ppm. Ding's group fabricated a fluorescent sensor with glutathione-protected

Yuying Zhang and Jianfang Qin contributed equally to this work.

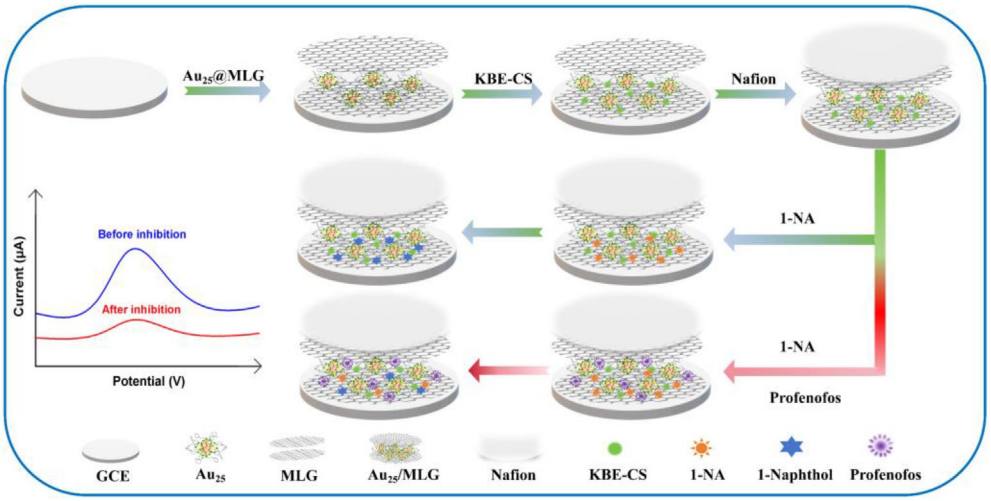

SCHEME 1 | Fabrication process of the NF/KBE-CS/Au_{25}@MLG/GC electrode.

Ag_{14} nanoclusters, which enabled the specific recognition of lysozyme and the detection of Hg^{2+} with high sensitivity. Despite atomically precise nanoclusters exhibiting a wide potential in photochemical sensing, the exploitation of metal nanoclusters in electrochemical sensors has scarcely been reported to date.

On the other hand, gold nanoparticles (AuNPs) have been widely utilized as the electrode material in electrochemical sensors, primarily owing to their advantages of low toxicity, high reactivity, and good biocompatibility [26–29]. Traditionally, these AuNPs sensors are constructed through the method of electrochemical deposition. In this depositional process, although electrochemical parameters, such as potential, current density, time, electrolyte composition, and temperature, can be precisely adjusted, the kinetics of diffusion and reduction for metal ions and their subsequent nucleation are difficult to manipulate, which thus brings a significant challenge to generate the deposited layers with perfect uniformity [30]. In fact, some inhomogeneous nanoparticles are often formed and randomly distributed on the electrode surface. Consequently, such structural nonuniformity would compromise the sensing performance, such as sensitivity and linear range fluctuations, noise increase, and poor reproducibility. Therefore, it is necessary to develop new types of nanomaterials to construct the uniformed electrochemical electrode with enhanced sensing capability.

To address the above issues, we consider employing atomic-precision gold nanoclusters as electrode materials, which enables the precise control of the interface at the nanoscale and thereby develops high-performance electrochemical sensors. In this work, well-defined Au_{25} nanoclusters were utilized to fabricate a three-layer KBE-CS/Au_{25}@MLG/GC electrode, where KBE, CS, MLG, and GC represent kidney bean enzyme, chitosan, multilayer graphene, and glassy carbon, respectively. The electrochemical electrode fabrication is summarized in Scheme 1. This fabricated cluster-based sensor was further optimized and exhibited a wide linear range and a high sensitivity for profenofos detection. In addition, the sensing mechanism, reproducibility, anti-interference, and stability of this biosensor were systematically evaluated in sequence. Finally, we carried out the pesticide detection of real samples to check out the practicality of the cluster-based biosensor.

2 | Results and Discussion

2.1 | Fundamental Properties of $Au_{25}(PET)_{18}$ Nanoclusters

The geometric structure of $Au_{25}(PET)_{18}$ (PET = 2-phenylethanethiol) nanocluster has been successfully resolved using x-ray crystallography by Jin's group [31]. Briefly, $Au_{25}(PET)_{18}$ nanocluster contains a core-shell framework, which consists of an $Au@Au_{12}$ icosahedron (core) and six dimeric $Au_2(SR)_3$ staples (shell), as depicted in Figure 1. The UV–vis–NIR spectrum of as-synthesized nanoclusters shows three prominent absorption peaks centered at 400, 455, and 680 nm (Figure S1), which agrees well with the fingerprint peaks of reported $Au_{25}(PET)_{18}$ and thus verifies the purity of the sample. Transmission electron microscopy (TEM) further reveals that $Au_{25}(PET)_{18}$ nanoclusters exhibit a uniform and monodisperse size of approximately 2 nm (Figure S2).

2.2 | Fundamental Properties of Modified Electrodes

The surface morphology of the fabricated NF/KBE-CS/Au_{25}@MLG/GC electrode was characterized using scanning electron microscopy (SEM). As shown in Figure 2A, the electrode surface exhibits a distinct multilayered graphene structure. The loading of Au_{25} nanoclusters did not alter the surface morphology of the electrode. Further, energy dispersive spectroscopy (EDS) analysis revealed that Au and S elements were uniformly distributed across the electrode surface (Figure 2B), confirming the successful and uniform loading of Au_{25} nanoclusters onto the multilayered graphene support.

Prior to evaluating the analytical performance of modified electrodes in detection systems, the standard probe system of $K_3[Fe(CN)_6]/K_4[Fe(CN)_6]$ is typically employed for the

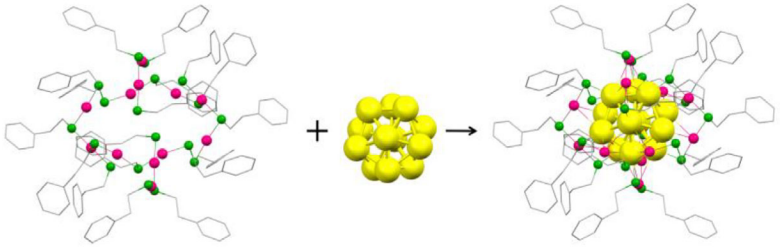

FIGURE 1 | Structural anatomy of $Au_{25}(PET)_{18}$ cluster. Color labels: Yellow/Magenta = Au; Green = S; Grey = C. H atoms are omitted for clarity.

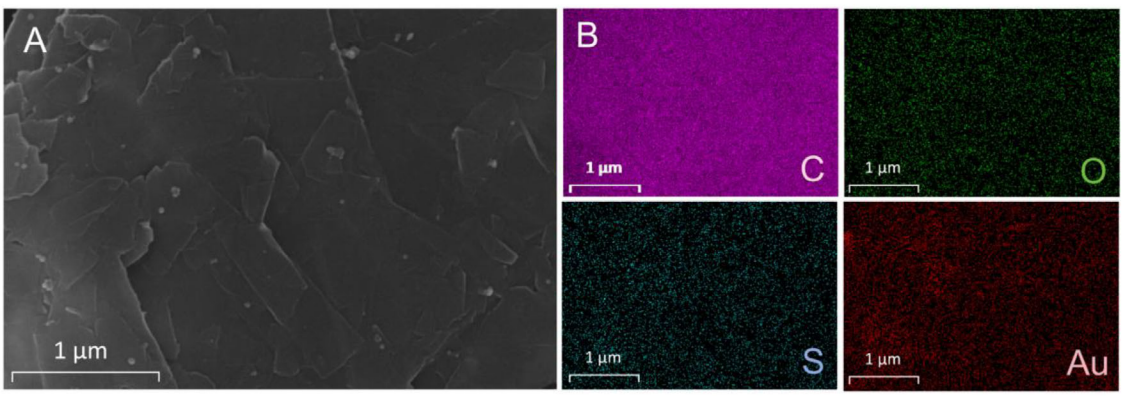

FIGURE 2 | (A) SEM and (B) EDS images of NF/KBE-CS/Au_{25}@MLG/GC electrode.

systematic characterization of electrode interfaces at different modification stages. This reversible redox couple serves as a sensitive electrochemical probe that effectively reveals the evolutionary patterns of the electrode interface microenvironment during sequential modification processes. By analyzing the differences in peak current and peak potential in CV curves, the conductive properties and interfacial mass transfer behavior of the modified materials can be elucidated, thereby validating the successful fabrication of the electrode interface. The as-fabricated biosensors were further characterized by cyclic voltammetry (CV) and electrochemical impedance spectroscopy (EIS). Specifically, every electrode shows a pair of reversible redox peaks in the potential range from −0.2 to 0.8 V due to the interconversion reaction of $[Fe(CN)_6]^{3-}/[Fe(CN)_6]^{4-}$. The original GC electrode exhibits a relatively high redox peak current, which obviously decreases after loading Au_{25}@MLG on the surface. Additionally, the redox peak potential and current of Au_{25}@MLG/GC are distinguished from those of Au_{25}/GC and MLG/GC electrodes, indicating the dependence of electron transport efficiency on loaded materials with different conductivities. The KBE-CS modification led to a further decrease in the redox current owing to the electron transfer barrier within KBE and CS. As expected, the immobilization of the NF layer results in the redox process being completely inhibited, since the negative-charged NF membrane made the electrode inaccessible for $Fe[(CN)_6]^{3-/4-}$ in solution due to the electrostatic repulsion (Figure 3A).

The above conclusions were supported by EIS, which can effectively measure the characteristic resistance of the electron transfer process at the electrode interface by Nyquist complex plane plots. As shown in Figure 3B, the charge transfer resistance (R_{ct}) of the as-fabricated electrodes follows the order of GC < Au_{25}/GC < Au_{25}@MLG/GC < MLG/GC < KBE-CS/Au_{25}@MLG/GC < NF/KBE-CS/Au_{25}@MLG/GC, which further demonstrates the inhibition of charge transfer by modified materials on the electrode surface.

2.3 | Electrochemical Response of the Modified Electrodes

Square wave voltammetry (SWV) measurements were performed to characterize the electrochemical response of the modified electrodes in PBS solution containing 1-naphthyl acetate (1-NA). It should be noted that 1-NA can be converted to 1-naphthol under enzyme catalysis (KBE), which can be further electro-oxidized to exhibit a corresponding oxidation peak by other heterogeneous catalysts, that is, the Au_{25} cluster in this work. In the SWV spectra, Au_{25}-, MLG-, and Au_{25}@MLG-modified electrodes demonstrate similar oxidation peaks around the potential of 0.43 V, and their peak currents are higher than that of the original GC electrode (~0.40 V), as shown in Figure 3C. These results preliminarily indicate the synergistic catalysis between the enzyme and other catalysts. Additionally, the highest peak current in NF/KBE-CS/Au_{25}@MLG/GC electrode implies the optimum synergy of the enzyme with Au_{25}@MLG due to the combination of the excellent conductivity of MLG and the electrocatalytic activity of Au_{25} nanocluster. Obviously, the higher oxidation peak current presents the better synergy of the two catalysts.

Undoubtedly, the modification of KBE is essential to the electrode due to its vital role in 1-NA transformation to 1-naphthol (Figure 3D). Both NF/KBE-CS/Au_{25}@MLG/GC and NF/KBE/Au_{25}@MLG/GC electrodes exhibit no obvious response in the absence of 1-NA in PBS solution, indicating the necessity of

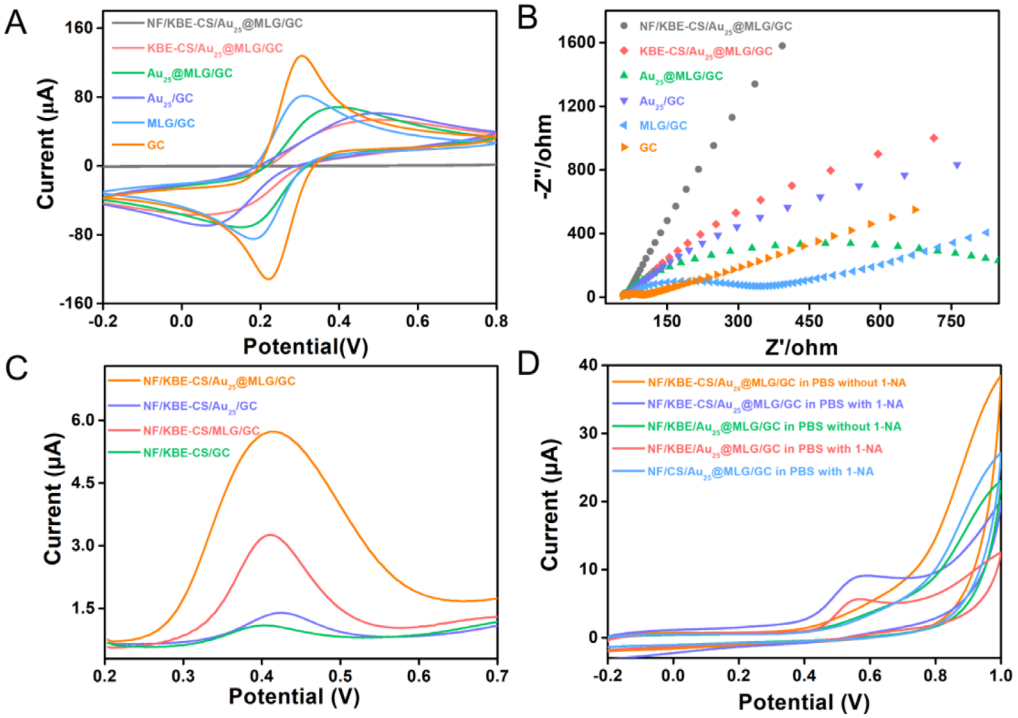

FIGURE 3 | (A) CV and (B) EIS curves for the electrodes with different modifications; (C) SWV curves in 1-NA-containing PBS solution for the modified electrodes; (D) CV curves of the modified electrodes in PBS solution in the presence/absence of 1-NA.

1-NA to the electrocatalysis system. By comparing the oxidation peak current of the CV curve for NF/KBE-CS/Au_{25}@MLG/GC and NF/KBE/Au_{25}@MLG/GC electrodes, it is readily concluded that the presence of CS is also necessary, since its antibacterial capability can protect the plant-esterase activity and thus facilitate the current response. To sum up, the modified NF/KBE-CS/Au_{25}@MLG/GC electrode is selected to optimize electrocatalytic behavior and thus serves as a biosensor for chemical detection.

2.4 | Condition Optimization and Mechanism Investigation

It is generally acknowledged that the amount of Au_{25}@MLG on the modified electrode and incubation time in the profenofos solution would significantly affect its behavior as a biosensor. These two factors are thus systematically evaluated to optimize the conditions. As depicted in Figure 4A, the response current of the NF/KBE-CS/Au_{25}@MLG/GC electrode exhibited an obvious increase with the amount of Au_{25}@MLG from 3 to 5 μL, which was followed by a decrease from 5 to 7 μL in 1-NA-containing PBS solution (pH = 7). On the other hand, the oxidation current is gradually inhibited with the increase of incubation time for the NF/KBE-CS/Au_{25}@MLG/GC electrode (Figure 4B). This inhibition effect reaches the maximum at the incubation time of 15 min, since all active sites in the enzyme have been almost occupied by the pesticide. Therefore, the optimized amount of Au_{25}@MLG and incubation time were respectively determined to be 5 μL and 15 min.

The oxidation process of 1-NA is essential to the biosensor of NF/KBE-CS/Au_{25}@MLG/GC, which can be systematically investigated by CV. As shown in Figure 5A, when the scanning rates vary from 50 to 500 $mV{\cdot}s^{-1}$, the response current increases apparently and the oxidation peak gradually shifts to the positive potential. The linear equation between the scanning rate (v) and the oxidation peak current (I_{pa}) is fitted to be I_{pa} = 8.347v–1.331 with a correlation coefficient R^2 = 0.998 (Figure 5B). The linear proportionality of peak current to scan rate confirms an adsorption-controlled, surface-confined electrode reaction [32–34].

Specifically, under adsorption control, the increased scanning rate promotes more reactant molecules to reach the electrode interface effectively and participate in electrochemical reactions, leading to a higher current. In addition, a CV diagram was obtained using NF/KBE-CS/Au_{25}@MLG/GC electrode at a scanning rate of 0.45 $mV{\cdot}s^{-1}$ in 0.1 mol/L PBS solution (pH = 7.0). According to the formula as follows, the electron transfer number ($n \approx 1$) was calculated [35], indicating that the redox reaction involves one electron transfer (Figure S3).

$$E_p - E_h = \frac{47.4}{n\alpha_S}$$

where E_p represents the peak potential, E_h is the half-wave potential, denotes the electron transfer coefficient, and n stands for the number of electrons transferred.

Subsequently, CV curves of the electrodes were collected in 1-NA solutions at different pH values. Exposure to both acid and alkali substances may lead to enzyme inactivation. Therefore, the relationship between the peak potential of oxidation peak (E_{pa})

and the pH of the solution ranging from 5.0 to 7.5 was investigated, as shown in Figure 5C. It is found that there is a good linear relationship between E_{pa} and pH, and the linear equation is as follows: $E_{pa} = 0.8503 - 0.0581$ pH with a slope of 58.1 mV/pH, which is close to 59 mV/pH (Figure 5D). The results show that the ratio between protons involved in the oxidation of 1-naphthol and transferred electrons is 1:1, so the oxidation process of the electrode is irreversible, and the transfer of electrons and protons is considerable [35].

2.5 | Performance Analysis of Sensors

The concentration of profenofos was detected by the sensor under optimal experimental conditions to analyze and evaluate the performance of the sensor. The SWV diagrams of the optimum biosensor before and after incubating in the profenofos were revealed in Figure 5E. It can be observed that the I_{cat} of the sensor decreased after incubation with profenofos, and the current decreased gradually with the increase of the concentration of profenofos. This phenomenon is mainly caused by the pesticide inhibiting the activity of plant enzymes, resulting in changes in the response current. In addition, there is a good linear relationship between the mass concentration of profenofos (lgC) and the inhibition rate (Inh %), ranging from 1 to 2000 μg/L, and the linear equation was as follows: Inh % = 15.76 lgc + 9.63, with the correlation coefficient R^2 of 0.98 (Figure 5F). The sensitivity of the sensor was 15.76/lgc, and the detection limit was identified to be 0.137 μg/L calculating by seven detections in blank solution. Owing to the rational design of the Au_{25}@MLG composite material, the NF/KBE-CS/Au_{25}@MLG/GC sensor constructed in this work exhibits a broader linear range and a lower limit for profenofos detection compared with other sensors reported in the literature [36–40].

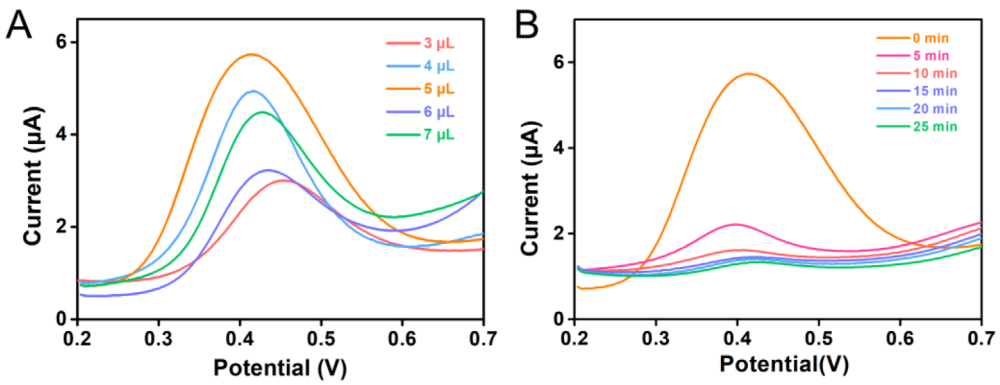

FIGURE 4 | SWV curves of NF/KBE-CS/Au_{25}@MLG/GC electrode with (A) various amounts of Au_{25}@MLG, (B) various inhibition times in the profenofos solution.

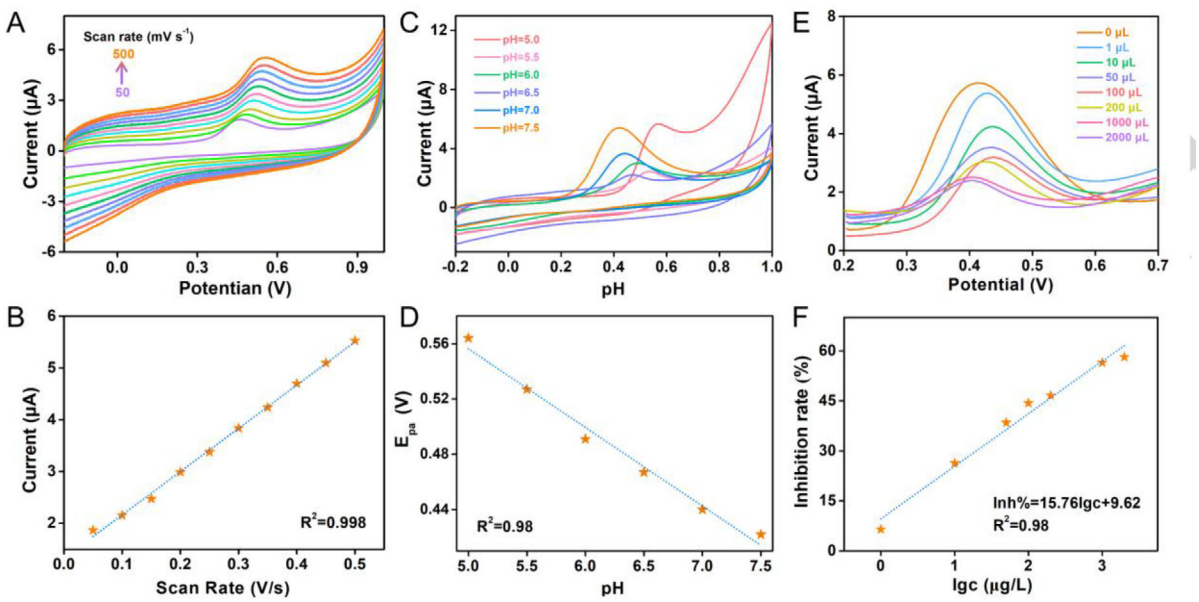

FIGURE 5 | (A) CV curves of NF/KBE-CS/Au_{25}@MLG/GC electrode at the scan rate range of 50~500 mV·s^{-1}. (B) Linear relationship between current and scan rate for NF/KBE-CS/Au_{25}@MLG/GC electrode. (C) CV curves of NF/KBE-CS/Au_{25}@MLG/GC electrode in 1-NA-containing PBS solution with the varied pH from 5 to 7.5; (D) Linear relationship between E_{pa} and pH; (E) SWV curves of NF/KBE-CS/Au_{25}@MLG/GC electrode incubated in PBS solution with the profenofos concentration range of 0~2000 μg/L for 15 min; (F) Linear relationship between profenofos concentration and inhibition rate.

2.6 | Reproducibility, Stability, Anti-interference, and Applicability of the Sensor

To evaluate the reproducibility of the fabricated sensor, seven modified electrodes were evaluated under the same conditions. As depicted in Figure S4, the difference in response current for these seven electrodes is within 5%, indicating that the electrochemical enzyme sensor has good reproducibility. The detection stability was further evaluated by repeating the profenofos detection seven times under an NF/KBE-CS/Au_{25}@MLG/GC sensor. The results showed no obvious decrease in the response current, demonstrating the excellent stability for the NF/KBE-CS/Au_{25}@MLG/GC sensor (Figure S5). The storage stability of the biosensor was also verified (Figure S6). Additionally, a variety of potential interfering substances, such as Na^+/Cu^{2+}/Zn^{2+}/Fe^{3+}/Pb^{2+} ions, sucrose, and oxalic acid, were added to the solutions together with profenofos. The experimental results demonstrated the outstanding anti-interference ability for the electrochemical electrode of NF/KBE-CS/Au_{25}@MLG/GC. For example, under the interference of inorganic ions (Na^+, Cu^{2+}, Zn^{2+}, and Fe^{3+}), the response signals could maintain above 95%, as shown in Figure S7. The above reproducibility, stability, and anti-interference for the fabricated electrode lay the foundation for the application in real conditions. Indeed, tap water and salt-lake water (Yuncheng City) served as the real sample to test the practicality of NF/KBE-CS/Au_{25}@MLG/GC electrode. As shown in Table S1, all the recovery rates all fell within the range of 100 ± 5%, with RSD below 4.8%, indicating that the sensor can detect the profenofos accurately. These results demonstrate the promising potential of this biosensor for pesticide detection in water samples.

3 | Conclusion

To summarize, we have exploited atomically precise nanoclusters as the electrode material to construct a high-performance electrochemical biosensor for the first time. In this electrode, multilayer graphene was employed to load Au_{25} nanoclusters, which significantly facilitated electron transfer and provided an ideal matrix to immobilize the plant enzyme. The fabricated NF/KBE-CS/Au_{25}@MLG/GC biosensor was optimized and demonstrated exceptional performance for profenofos detection with a wide linear range (1~2000 μg/L) and a low detection limit (0.137 μg/L). In addition, the outstanding reproducibility, stability, and anti-interference capability were sequentially validated, which thereby assures the practical applicability of this biosensor in real environmental water samples. Overall, the fabrication of cluster-based biosensors not only extends the application of the sensing field for well-defined nanoclusters but also provides a novel strategy for the development of next-generation, high-performance sensing devices in environmental monitoring.

4 | Experimental Section

4.1 | Preparation of $Au_{25}(PET)_{18}$ Nanoclusters

$Au_{25}(PET)_{18}$ (PET = 2-phenylethanethiol) nanoclusters were synthesized according to the reported method [31]. Specifically, tetra-*n*-octylammonium bromide (TOAB, 675 mg) was dissolved in 30 mL of tetrahydrofuran (THF) under vigorous stirring (1000 rpm), which was followed by the addition of $HAuCl_4$ (496 mg dissolved in 5 mL of THF). This mixture was continuously stirred for 30 min. The stirring rate was decreased to 100 rpm. And 1020 μL of PET ligand was then dropped into the flask under an ice bath. The reaction solution turns colorless after 3 h, and the stirring rate was increased to 1000 rpm. Subsequently, a freshly prepared $NaBH_4$ solution (536 mg in 8 mL of cold water) was added to the solution at once. The reaction was carried out overnight (12~16 h). The resultant solution was concentrated into 5 mL by vacuum rotary evaporation, which was washed with methanol five times to remove impurities. The obtained precipitates were redissolved in the mixture solution (toluene/methanol = 1/4). The needle-like crystals of $Au_{25}(PET)_{18}$ were cultivated by liquid phase diffusion after 24 h.

4.2 | Preparation of Au_{25}@MLG Suspension

MLG (10 mg), purchased from Aladdin, was ultrasonically dispersed in 10 mL of N, N-dimethylformamide. 4 mL of MLG suspension was then mixed with a freshly prepared $Au_{25}(PET)_{18}$ solution (1 mg in 1 mL of N, N-dimethylformamide) to prepare Au_{25}@MLG suspension.

4.3 | Preparation of KBE-CS Solution

KBE was extracted by the method of water extraction. Briefly, quantitative white kidney beans were fully crushed and mixed with ultra-pure water in a certain proportion. The above solution was stirred vigorously and then stored in the refrigerator overnight, which was followed by centrifugation. The obtained supernatant contained the KBE. KBE-CS solution was obtained by mixing 1 mg of CS with 5 mL of KBE.

4.4 | Preparation of 1-NA Solution

1-NA (0.0745 g) was dissolved in 5 mL of ethanol. Subsequently, 5 mL of PBS buffer solution (pH = 7.0) was mixed with 50 μL of the above solution to obtain 1-NA solution (0.8 mmol/L).

4.5 | Preparation of Nafion Solution

The Nafion solution (NF, 0.5%) was prepared by mixing 10 μL of NF (5%) solution with 90 μL of anhydrous ethanol.

4.6 | Fabrication of NF/KBE-CS/Au_{25}@MLG/GC Biosensor

The surface of GC electrode was polished by using alumina powder with dimensions of 0.3 and 0.05 μm, respectively, which was followed by water washing and drying. The clean GC electrode was then coated with quantitative Au_{25}@MLG suspension and

dried by standing. The volume of Au_{25}@MLG suspension varied from 3 to 7 μL to optimize the conditions. After that, 10 μL of KBE-CS and 4 μL NF (0.5%) solutions were successively dropped onto the electrode surface to construct NF/KBE-CS/Au_{25}@MLG/GC. Notably, the electrode surface should be dried after the addition of each solution. The comparative electrodes of NF/KBE-CS/Au_{25}/GC, NF/KBE-CS/MLG/GC, and NF/KBE-CS/GC were separately prepared by a similar approach.

4.7 | Characterizations

UV–vis–NIR spectroscopy of gold nanoclusters was performed on a Cary5000 spectrophotometer (Agilent) with a range of 250~800 nm. SEM (Hitachi, S-4800) was employed to characterize the morphology of the as-fabricated GC electrode. TEM (JEOL, JEM-F200) was used to characterize the morphology and size of the cluster.

All electrochemical measurements were carried out on a CHI760e electrochemical workstation (Shanghai Chenhua Instrument) with a three-electrode system, in which the as-fabricated GC, Pt wire, and Ag/AgCl serve as working electrode, counter electrode, and reference electrode, respectively. CV and EIS were tested in electrolyte (5 mM $[Fe(CN)_6]^{3-/4-}$ and 0.1 M KCl) to verify the modified electrode with the scanning range from −0.2 to 0.8 V. SWV was preformed to explore the electrocatalytic activities of the as-fabricated electrode in the mixture of 0.1 M PBS and 0.8 mM 1-NA solutions, with the scanning range from 0.2 to 0.7 V and the amplitude of 0.025 V. The sensing performance was evaluated by the inhibition ratio (Inh %) of profenofos to the enzyme-modified electrode, which was calculated by the following equation:

$$\text{Inh}\,\% = \frac{(I_0 - I)}{I_0} \times 100$$

where I_0 and I refer to the SWV peak current before and after incubation in profenofos-containing solution, respectively.

The biosensor applicability was evaluated by detecting the content of profenofos in real water samples, including tap water from Yuncheng City and lake water from the Yuncheng Salt Lake. A series of concentrations (5×10^{-6}, 100×10^{-6}, and 1000×10^{-6} μg/L) of profenofos were introduced into the real water samples to simulate contamination. SWV detection was carried out under the experimental conditions optimized previously after a 15 min incubation of the biosensor in the as-prepared sample. The concentration of profenofos in each sample was determined based on the established calibration curve. The recovery rate was then calculated using the following formula to assess the accuracy of the method.

$$\text{Recovery}\,(\%) = \frac{\text{Measured concentration}}{\text{Spiked concentration}} \times 100\%$$

Acknowledgments

This work was supported by the Shanxi Provincial Basic Research Program (No. 202303021222244, 202403021221205, 202403021222301), the PhD Research Launch Project of Yuncheng University (No. YQ-2023022, YQ-2024014), the Outstanding Doctoral Research Project in Shanxi (No. QZX-2023008, LJZX-202515), the Scientific and Technological Innovation Program of Higher Education Institutions in Shanxi (No. 2024L331) and the Scientific Research and Innovation Team Construction Program of Yuncheng University (YCXYTD-202403, YCXYTD-202404).

Conflicts of Interest

The authors declare no conflicts of interest.

Data Availability Statement

The data that supports the findings of this study are available in the supplementary material of this article.

References

1. R. C. Jin, C. J. Zeng, M. Zhou, and Y. X. Chen, "Atomically Precise Colloidal Metal Nanoclusters and Nanoparticles: Fundamentals and Opportunities," *Chemical Reviews* 116 (2016): 10346–10413, https://doi.org/10.1021/acs.chemrev.5b00703.

2. T. Higaki, Y. W. Li, S. Zhao, et al., "Atomically Tailored Gold Nanoclusters for Catalytic Application," *Angewandte Chemie International Edition* 58 (2019): 8291–8302, https://doi.org/10.1002/anie.201814156.

3. I. Chakraborty and T. Pradeep, "Atomically Precise Clusters of Noble Metals: Emerging Link Between Atoms and Nanoparticles," *Chemical Reviews* 117 (2017): 8208–8271, https://doi.org/10.1021/acs.chemrev.6b00769.

4. K. D. Gilroy, A. Ruditskiy, H. C. Peng, D. Qin, and Y. Xia, "Bimetallic Nanocrystals: Syntheses, Properties, and Applications," *Chemical Reviews* 116 (2016): 10414–10472, https://doi.org/10.1021/acs.chemrev.6b00211.

5. G. Y. Ma, F. Sun, L. Qiao, et al., "Atomically Precise Alkynyl-protected $Ag_{20}Cu_{12}$ Nanocluster: Structure Analysis and Electrocatalytic Performance Toward Nitrate Reduction for NH_3 Synthesis," *Nano Research* 16 (2023): 10867–10872, https://doi.org/10.1007/s12274-023-5885-6.

6. Q. Li, K. J. Lambright, M. G. Taylor, et al., "Reconstructing the Surface of Gold Nanoclusters by Cadmium Doping," *Journal of the American Chemical Society* 139 (2017): 17779–17782, https://doi.org/10.1021/jacs.7b11491.

7. X. Cai, W. G. Hu, S. Xu, et al., "Structural Relaxation Enabled by Internal Vacancy Available in a 24-Atom Gold Cluster Reinforces Catalytic Reactivity," *Journal of the American Chemical Society* 142 (2020): 4141–4153, https://doi.org/10.1021/jacs.9b07761.

8. X. Liu, G. Saranya, X. Y. Huang, et al., "$Ag_2Au_{50}(PET)_{36}$ Nanocluster: Dimeric Assembly of $Au_{25}(PET)_{18}$ Enabled by Silver Atoms," *Angewandte Chemie International Edition* 59 (2020): 13941–13946, https://doi.org/10.1002/anie.202005087.

9. X. Liu, W. W. Xu, X. Y. Huang, et al., "De Novo Design of $Au_{36}(SR)_{24}$ Nanoclusters," *Nature Communications* 11 (2020): 3349, https://doi.org/10.1038/s41467-020-17132-5.

10. X. Cai, G. Saranya, K. Q. Shen, et al., "Reversible Switching of Catalytic Activity by Shuttling an Atom Into and Out of Gold Nanoclusters," *Angewandte Chemie International Edition* 58 (2019): 9964–9968, https://doi.org/10.1002/anie.201903853.

11. C.-A. J. Lin, T. Y. Yang, C. H. Lee, et al., "Synthesis, Characterization, and Bioconjugation of Fluorescent Gold Nanoclusters Toward Biological Labeling Applications," *ACS Nano* 3 (2009): 395–401, https://doi.org/10.1021/nn800632j.

12. C. J. Zeng, T. Li, A. Das, N. L. Rosi, and R. C. Jin, "Chiral Structure of Thiolate-Protected 28-Gold-Atom Nanocluster Determined by x-ray Crystallography," *Journal of the American Chemical Society* 135 (2013): 10011–10013, https://doi.org/10.1021/ja404058q.

13. T. X. Song, C. Y. Shen, Y. Q. Tian, Q. X. Zhai, S. S. Tang, and Y. Zhu, "A Heterodimeric Cluster-Based Pair Catalyst for Electrochemical Synthesis of Cyclohexanone Oxime," *Angewandte Chemie International Edition* 64 (2025): e202507569, https://doi.org/10.1002/anie.202507569.

14. X. Cai, H. Wang, Y. Q. Tian, W. P. Ding, and Y. Zhu, "Catalytic Application of Atomically Precise Metal Clusters in Selective Hydrogenation Processes," *ACS Catalysis* 14 (2024): 11918–11930, https://doi.org/10.1021/acscatal.4c02965.

15. Q. Yuan, T. C. Li, H. Q. Lin, et al., "Toward the Customized Performance on a Supported Au_4Ru_2 Cluster Catalyst," *Advanced Functional Materials* 35 (2025): 2424623.

16. X. Liu, J. Tang, F. M. Zhao, et al., "Atomically Engineered Trimetallic Nanoclusters towards Enhanced Photoluminescence and Photoinitiation Activity," *Advanced Materials* 37 (2025): 2417984.

17. G. Li and R. C. Jin, "Gold Nanocluster-Catalyzed Semihydrogenation: A Unique Activation Pathway for Terminal Alkynes," *Journal of the American Chemical Society* 136 (2014): 11347–11354, https://doi.org/10.1021/ja503724j.

18. S. Jin, W. Liu, D. Q. Hu, et al., "Aggregation-Induced Emission (AIE) in Ag–Au Bimetallic Nanocluster," *Chemistry—A European Journal* 24 (2018): 3712–3715, https://doi.org/10.1002/chem.201800189.

19. Z. Tang, B. Xu, B. Wu, D. A. Robinson, N. Bokossa, and G. Wang, "Monolayer Reactions of Protected Au Nanoclusters With Monothiol Tiopronin and 2,3-dithiol Dimercaptopropanesulfonate," *Langmuir* 27 (2011): 2989–2996, https://doi.org/10.1021/la1045628.

20. J. Yoshimoto, A. Sangsuwan, I. Osaka, et al., "Optical Properties of 2-Methacryloyloxyethyl Phosphorylcholine-Protected Au_4 Nanoclusters and Their Fluorescence Sensing of C-reactive Protein," *Journal of Physical Chemistry C* 119 (2015): 14319–14325, https://doi.org/10.1021/acs.jpcc.5b03934.

21. X. Jia, X. Yang, J. Li, D. Li, and E. Wang, "Stable Cu Nanoclusters: From an Aggregation-Induced Emission Mechanism to Biosensing and Catalytic Applications," *Chemical Communications* 50 (2014): 237–239, https://doi.org/10.1039/C3CC47771A.

22. Y. Wang, Y. Wang, F. Zhou, P. Kim, and Y. Xia, "Protein-Protected Au Clusters as a New Class of Nanoscale Biosensor for Label-Free Fluorescence Detection of Proteases," *Small* 8 (2012): 3769–3773, https://doi.org/10.1002/smll.201201983.

23. J. Zhang, Y. Yuan, G. L. Liang, et al., "A Microwave-facilitated Rapid Synthesis of Gold Nanoclusters With Tunable Optical Properties for Sensing Ions and Fluorescent Ink," *Chemical Communications* 51 (2015): 10539–10542, https://doi.org/10.1039/C5CC03086B.

24. W. H. Ding, L. M. Guan, J. J. Han, R. Mangala, and Z. C. Luo, "Fluorescence Chemosensing of Water-Soluble Ag_{14} Nanoclusters for Lysozyme and Hg^{2+} Ions," *Sensors and Actuators B: Chemical* 250 (2017): 364–371, https://doi.org/10.1016/j.snb.2017.04.172.

25. A. George, E. Shibu, S. M. Maliyekkal, M. Bootharaju, and T. Pradeep, "Luminescent, Freestanding Composite Films of Au_{15} for Specific Metal Ion Sensing," *ACS Applied Materials & Interfaces* 4 (2012): 639.

26. Y. Peng, S. Ou, M. L. Li, Z. Q. Hu, Z. Zeng, and N. H. Feng, "An Electrochemical Biosensor Based on Network-Like DNA Nanoprobes for Detection of Mesenchymal Circulating Tumor Cells," *Biosensors and Bioelectronics* 238 (2023): 115564, https://doi.org/10.1016/j.bios.2023.115564.

27. J. R. Guo, M. Y. Li, S. P. Long, et al., "Bio-inspired Electrochemical Detection of Nitric Oxide Promoted by Coordinating the Histamine-Iron Phthalocyanine Catalytic Center on Microelectrode," *Analytical Chemistry* 95 (2023): 8842–8849, https://doi.org/10.1021/acs.analchem.3c00299.

28. H. F. Cui, T. T. Zhang, Q. Y. Lv, X. J. Song, X. J. Zhai, and G. G. Wang, "An Acetylcholinesterase Biosensor Based on Doping Au Nanorod@SiO_2 Nanoparticles Into TiO_2-Chitosan Hydrogel for Detection of Organophosphate Pesticides," *Biosensors and Bioelectronics* 141 (2019): 111452, https://doi.org/10.1016/j.bios.2019.111452.

29. X. R. Zhang, Y. P. Xu, Y. Q. Yang, et al., "A New Signal-On Photoelectrochemical Biosensor Based on a Graphene/Quantum-Dot Nanocomposite Amplified by the Dual-Quenched Effect of Bipyridinium Relay and AuNPs," *Chemistry—A European Journal* 18 (2012): 16411–16418, https://doi.org/10.1002/chem.201202213.

30. T. Domenica, S. Erika, and G. Isacco, "Electrochemical Deposition of Nanomaterials for Electrochemical Sensing," *Sensors* 19 (2019): 1186.

31. M. Z. Zhu, C. M. Aikens, F. J. Hollander, G. C. Schatz, and R. C. Jin, "Correlating the Crystal Structure of a Thiol-Protected Au_{25} Cluster and Optical Properties," *Journal of the American Chemical Society* 130 (2008): 5883–5885, https://doi.org/10.1021/ja801173r.

32. A. J. Bard, L. R. Faulkner, and H. S. White, *Electrochemical Methods: Fundamentals and Applications* (World Publishing Corporation, 2020).

33. H. L. Hu and N. Li, *Electrochemical Measurement* (National Defence Industry Press, 2007).

34. J. R. Guo, M. Y. Li, S. P. Long, J. Zhu, P. Miao, and T. X. Wei, "Bio-Inspired Electrochemical Detection of Nitric Oxide Promoted by Coordinating the Histamine-Iron Phthalocyanine Catalytic Center on Microelectrode," *Analytical Chemistry* 95 (2023): 8842–8849, https://doi.org/10.1021/acs.analchem.3c00299.

35. P. K. Kalambate, B. J. Sanghavi, S. P. Karna, and A. K. Srivastava, "Simultaneous Voltammetric Determination of Paracetamol and Domperidone Based on a Graphene/Platinum Nanoparticles/Nafion Composite Modified Glassy Carbon Electrode," *Sensors and Actuators B: Chemical* 213 (2015): 285–294, https://doi.org/10.1016/j.snb.2015.02.090.

36. J. Han, Y. Y. Yu, G. J. Wang, et al., "Ultrasensitive Electrochemiluminescence Aptasensor Based on ABEI Reduced Silver Nanoparticles for the Detection of Profenofos," *Science of The Total Environment* 844 (2022): 157184, https://doi.org/10.1016/j.scitotenv.2022.157184.

37. C. Li, G. P. Zhang, S. Q. Wu, and Q. C. Zhang, "Aptamer-Based Microcantilever-Array Biosensor for Profenofos Detection," *Analytica Chimica Acta* 1020 (2018): 116–122, https://doi.org/10.1016/j.aca.2018.02.072.

38. N. Nesakumar, I. Suresh, G. B. Jegadeesan, J. B. B. Rayappan, and A. J. Kulandaiswamy, "An Efficient Electrochemical Sensing Platform for Profenofos Detection," *Measurement* 202 (2022): 111807, https://doi.org/10.1016/j.measurement.2022.111807.

39. H. Zhang, J. F. Sun, S. T. Cheng, et al., "A Dual-Amplification Electrochemical Aptasensor for Profenofos Detection," *Journal of The Electrochemical Society* 167 (2020): 027515, https://doi.org/10.1149/1945-7111/ab6972.

40. A. E. Radi, R. Oreba, and R. Elshafey, "Molecularly Imprinted Electrochemical Sensor for the Detection of Organophosphorus Pesticide Profenofos," *Electroanalysis* 33 (2021): 1945–1951, https://doi.org/10.1002/elan.202100175.

Supporting Information

Additional supporting information can be found online in the Supporting Information section.

Supporting File: Additional supporting information can be found online in the Supporting Information section. The supporting information includes supplementary Figures and Tables.